**Supplemental information for:**

# The influence of detachment strength on the evolving deformational energy budget of physical accretionary prisms

Jessica McBeck[1, 2], Michele Cooke[1], Pauline Souloumiac[3], Bertrand Maillot[3], Baptiste Mary[3]

[1] Department of Geosciences, University of Massachusetts Amherst, MA, USA
[2] Now at: Physics of Geological Processes, The Njord Centre, Department of Geosciences, University of Oslo, Norway
[3]Département Géosciences et Environnement, Université de Cergy-Pontoise, Cergy-Pontoise, France

## *Overview*

This supplemental information contains one section of text, and five figures. Text S1 describes our calculation of the effective stiffness of the wedges. Figure S1 shows the calibration of the machine units of the strain gauges to normal force measurements. Figure S2 shows the results of the calculation of effective stiffness of the experimental wedges. Figure S3 shows the kinematic compatibility assessment used to determine the robustness of the DIC fields. Figure S4 shows the cumulative slip distribution along faults. Figure S5 shows displacements fields from the top views of experiments with opposing configurations.

## *Supplemental Text S1:* Effective stiffness

In order to calculate the internal work done within the wedge, we must estimate the stress state within the wedge. We used Hooke's laws to estimate 2D stress tensors from strain tensors. These laws assume linear elasticity. Although the rheology of the sandpack within the fault zones is closer to plastic than linear elastic, it is reasonable to assume that the sand aggregate between the faults has a linear relationship between stress and strain. Preceding fault development, the stress-strain curves are approximately linear, indicating the linearity of this relationship.

To estimate the effective stiffness of the sand wedges, we calculated the normal stress exerted on the load-bearing area of the backwall and the horizontal longitudinal strain within the sandpacks preceding thrust faulting. We used the normal force measured on the backwall (Fig. 3) and an effective height of the load-bearing area of 4 cm, equal to the height of the rectangular sandpack. Calculating the horizontal contraction requires the displacement of the edge of the box and the length of the contracting region. We measured the horizontal displacement of the backwall recorded in the DIC displacement fields. We considered the full length of the sandbox (90 cm) as the length of the compacting region. Selecting a load-bearing height of 4 cm and contraction region length of 90 cm reflects the goal of calculating the effective stiffness throughout the wedge, and not only near the backwall or sidewalls. Although high magnitudes of horizontal compression are localized into different volumes in the experiments with opposing apparatus configurations (Fig. 9), the force exerted on the backwall was a result of force networks that span the length of the sandpack from the backwall to the opposite wall. From the horizontal displacement of the backwall observed in the DIC fields from both sides, we found the average of the strains from the left and right sides as representative of the strain.

These estimates of the effective stiffness (~1 MPa) (Fig. S2) exceed previous estimates (0.11-0.25 MPa) of the effective stiffness of wedges built with an UCP depositor (*Herbert*, 2014). The difference may arise because experiments presented here used the larger UCP depositor (~1.5 m x 1.5 m base), whereas *Herbert* (2014) use the smaller UCP depositor (0.65 m x 0.245 m base) to construct the analyzed sandpacks. The larger UCP depositor may produce sandpacks with more closely packed sand grains than the smaller depositor. Closer packing of grains would increase the effective bulk stiffness, because more densely packed grains inhibit grain rearrangement. Tests with the smaller UCP depositor demonstrate that the diameter, spacing, and number of holes in the depositor sieves, and the distance between the sand reservoir, adjacent sieves and the experimental box influence the resulting sandpack density (*Maillot*, 2013).

Laboratory uniaxial compression tests of dry sand aggregates estimate stiffness that exceed the estimates from these UCP experiments. Dry sand in uniaxial compression tests with 50 loading-unloading cycles has apparent stiffness ranging from 100-400 MPa in the first cycle (*Klinkmuller et al*., 2008, 2016). Geotechnical engineering studies provide additional constraints on the expected effective stiffness of aggregates of sand grains (e.g., *Roberston and Campanella,* 1983). Empirical relationships derived from normally consolidated sand produce estimates of effective stiffness at 50% failure stress from 10-50 MPa (*Baldi et al.*, 1981). However, the estimates of bulk stiffness from these tests will likely exceed the effective stiffness within experimental wedges, where the sandpack is unconfined and free to uplift. If the upward movement of the sand grains were restricted in the sandbox experiment, the applied backwall displacement would produce greater backwall force than in the present unconfined configuration, producing higher estimates of effective stiffness that would be closer to confined laboratory measurements.

## *Supplemental Figures*

### Figure S1

Calibration used to measure physical backwall force. A) Uniaxial strain sensors were mounted on four plaques that are fixed to a rigid board, which lay adjacent to the backwall in the experiments. Each plaque (blue) contained four uniaxial strain sensors (white rectangles) that are fixed to the two metal arms mounted on the plaque. B) Calibration of strain gauges to known weights resulted in a linear relationship of machine strain units to weight ($R^2$=0.99).

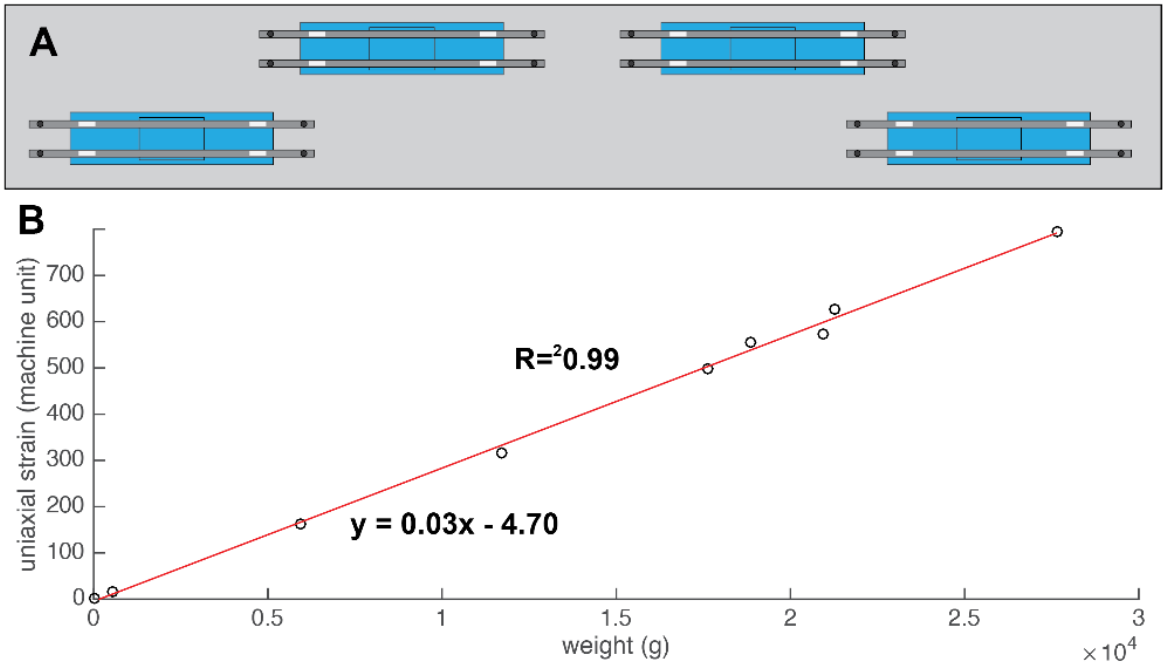

**Figure S2**

Estimates of effective stiffness of the physical accretionary wedges. A) Relationships between normal force exerted on backwall and backwall displacement measured from DIC fields from the top view camera. C) Resulting stress-strain relationships. Lines indicate tangent at 50% peak stress that determines the stiffness estimate. Linearity of the stress-strain curves suggest that using Hooke's laws provide a reasonable approximation of the stress state within the wedge outside of the fault zones.

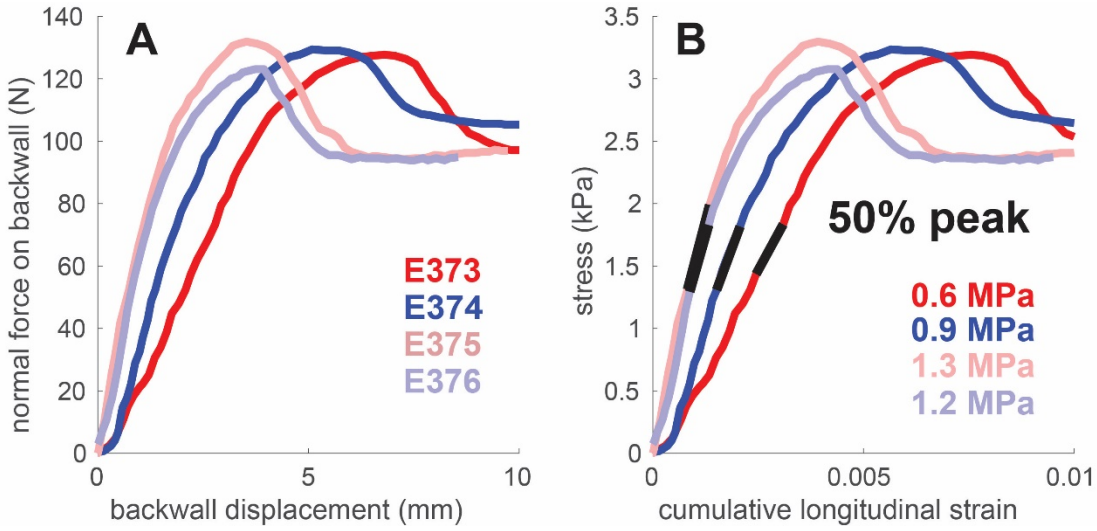

**Figure S3**

Kinematic compatibility of displacement fields indicates the amount of artificial noise in incremental displacement fields. Net displacement fields (A), and corresponding kinematic compatibility field (B) for example incremental displacement fields of left (upper row) and right (lower row) side of experiment E375. High *K* was produced locally along faults in the left side displacement field, and in regions with higher artificial noise in right side displacement field. C) Histogram of kinematic compatibility, *K,* field for left and right sides reveal that the right side had higher magnitudes of *K* than the left side. To compare the kinematic compatibility of each displacement field to other fields, we considered the mean plus one standard deviation of the *K* field as the kinematic compatibility value representing that field, $K^F$, shown as red lines in (C). D) From each kinematic compatibility field, we identified $K^F$, and removed the fields from the analysis that had $K^F$ above one standard deviation from the mean of all $K^F$ from each incremental displacement field. Models within the gray region were thus considered reliable. Triangles pointing to the left (black triangle) and right (white triangle) show $K^F$ of displacement fields derived from the left and right sides of the experimental apparatus, respectively. Most of the displacement fields from the right side of experiment E375 were considered unreliable due to inadequate focusing of the associated camera. Consequently, we excluded the incremental displacement fields calculated for the right side of experiment E375 from further analysis.

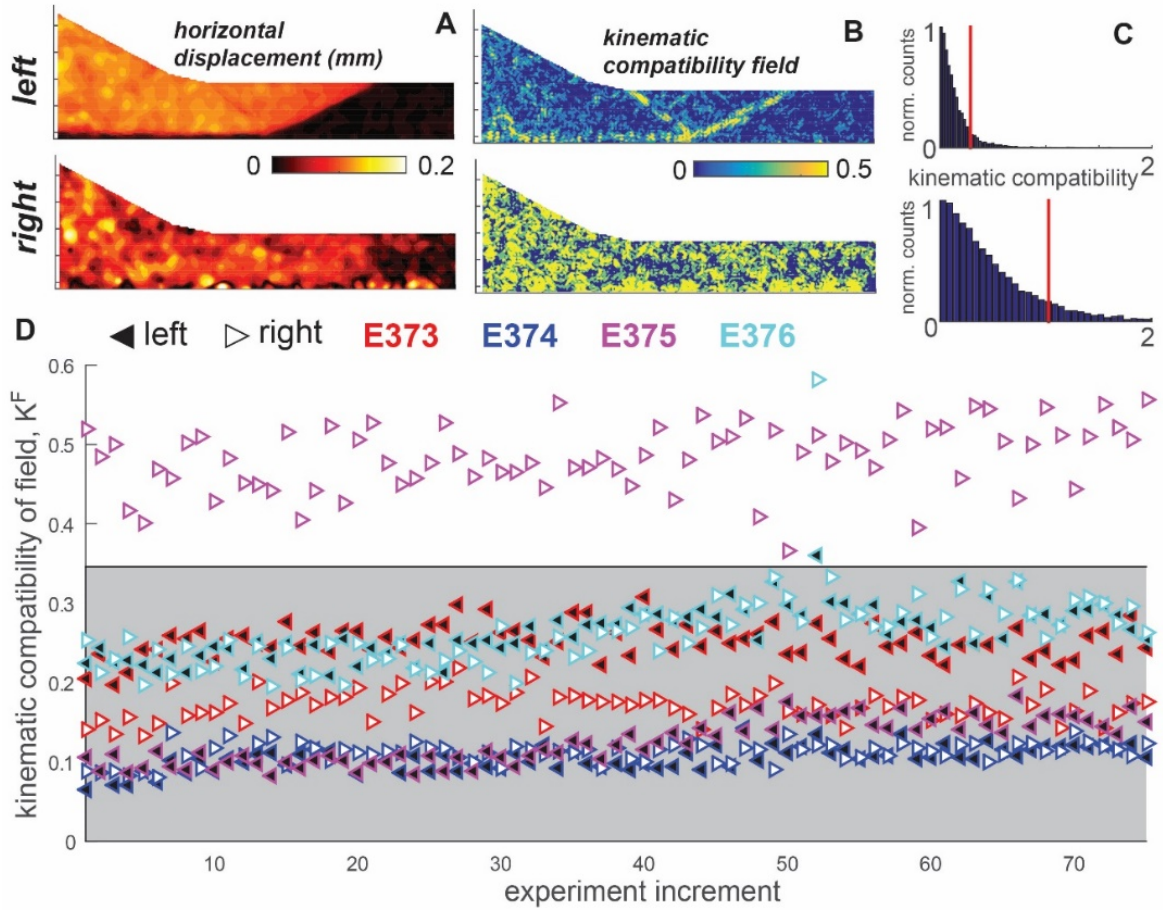

**Figure S4**

Cumulative slip distribution along detachment (black), backthrust (blue) and forethrust (red) in experiment with glass detachment (thicker lines) and sand detachment (thinner lines) at 6 mm of cumulative backwall displacement. Resulting contribution to $W_{fric}$ listed near corresponding fault. The higher slip and higher frictional coefficient of the detachment and lower slip on the backthrust in the glass detachment compared to the sand detachment experiment produced the lower frictional work in the glass detachment experiment relative to the sand detachment experiment.

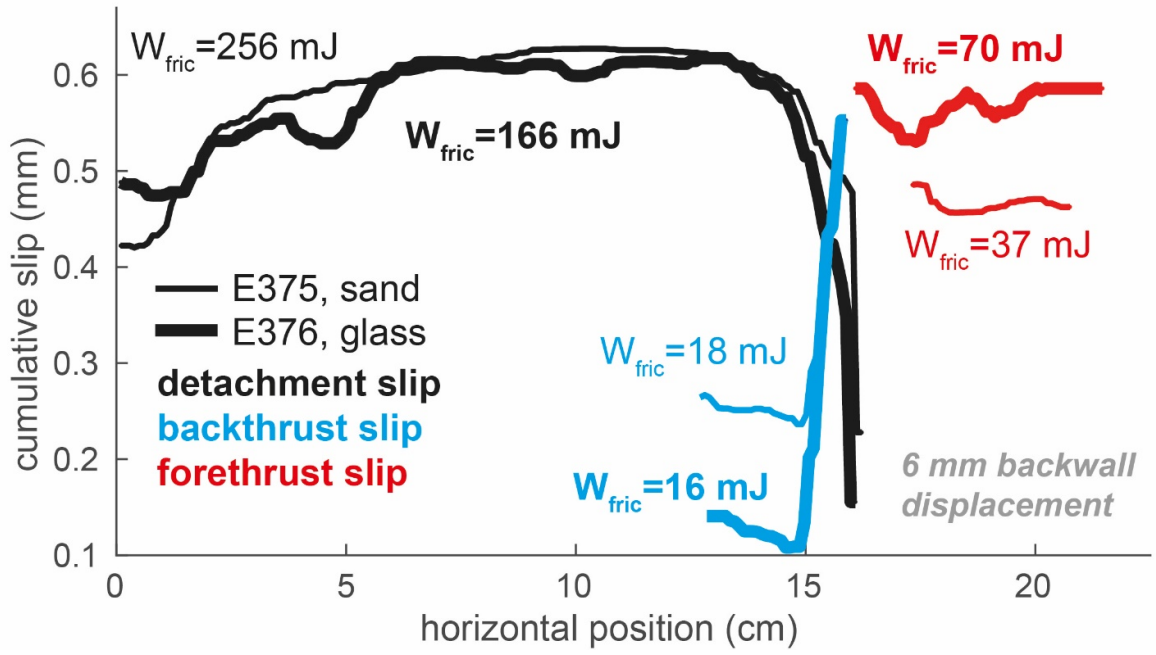

**Figure S5**

Net displacements from top views of experiment A) E374 (moving base), and B) E376 (moving backwall). Red numbers show the cumulative backwall displacement calculated from the side view DIC fields. The backwall is located at the bottom of each image. The motor is located at the top in the moving base (A) and at the bottom in the moving backwall (B) experiment. Following thrust fault development, the thrust fault strike is sub-perpendicular to the backwall in both experiments with differing apparatus configurations. Consequently, the impact of sidewall friction drag on thrust fault geometry is minimal after the thrusts have localized across the full width of the sandpack.